The Generation of Coronal Loop Waves below the Photosphere by *p*-Mode Forcing [1]

Bradley W. Hindman

JILA and Department of Astrophysical and Planetary Sciences, University of Colorado, Boulder, CO 80309-0440, USA

hindman@solarz.colorado.edu

Rekha Jain

Applied Mathematics Department, University of Sheffield, Sheffield S3 7RH, UK

ABSTRACT

Recent observations of coronal-loop waves by *TRACE* and within the corona as a whole by CoMP clearly indicate that the dominant oscillation period is 5 minutes, thus implicating the solar p modes as a possible source. We investigate the generation of tube waves within the solar convection zone by the buffeting of p modes. The tube waves—in the form of longitudinal sausage waves and transverse kink waves—are generated on the many magnetic fibrils that lace the convection zone and pierce the solar photosphere. Once generated by p-mode forcing, the tube waves freely propagate up and down the tubes, since the tubes act like light fibers and form a waveguide for these magnetosonic waves. Those waves that propagate upward pass through the photosphere and enter the upper atmosphere where they can be measured as loop oscillations and other forms of propagating coronal waves. We treat the magnetic fibrils as vertically aligned, thin flux tubes and compute the energy flux of tube waves that can generated and driven into the upper atmosphere. We find that a flux in excess of 10^5 ergs cm^{-2} s^{-1} can be produced, easily supplying enough wave energy to explain the observations. Furthermore, we compute the associated damping rate of the driving p modes and find that the damping is significant compared to observed line widths only for the lowest order p modes.

Subject headings: MHD — Sun: corona — Sun: helioseismology — Sun: magnetic fields — Sun: oscillations

1. Introduction

It is now well established through observations by the *Solar and Heliospheric Observatory* (*SOHO*), the *Transition Region and Coronal Explorer* (*TRACE*), and *Hinode* that the solar atmosphere supports the propagation of a variety of magnetohydrodynamic (MHD) waves. Slow magnetosonic waves have been implicated in the observations of coronal plumes (Ofman et al. 1997; Ofman, Nakariakov & DeForest 1999; DeForest & Gurman 1998) and in coronal-loop oscillations (e.g., Berghmans & Clette 1999; De Moortel, Ireland & Walsh 2000; De Moortel, Hood & Ireland 2002). Wang et al. (2002) interpreted oscillatory behavior seen in very

[1]This paper was originally published in the Astrophysical Journal on 10 April 2008, vol. 677, pp. 769–780

hot (> 5 MK) coronal loops by *SOHO*/SUMER, as standing slow magnetosonic waves of long wavelength. A propagating intensity oscillation with 5 minute periodicity in a "nonsunspot" coronal loop has also been reported by Marsh et al. (2003). They estimate a speed of 50–195 km s^{-1} for this wave and suggest, on the basis of Coronal Diagnostic Spectrometer (*SOHO*/CDS) data, that it is also present at chromospheric, transition region, and coronal temperatures.

Fast magnetosonic waves have also been invoked to explain coronal and chromospheric oscillation observations. Williams et al. (2002) report intensity fluctuations with a period of 6 s along and within coronal loops. The propagation speed is estimated to be 2×10^3 km s^{-1}, suggesting the possibility of fast magnetosonic waves. Verwichte, Nakariakov & Cooper (2005) have recently claimed to have seen propagating fast kink waves in a postflare supra-arcade. Transverse loop oscillations observed by *TRACE* (Aschwanden et al. 1999; Nakariakov et al. 1999) have also been linked to fast kink waves. Finally, there have been suggestions that the large-scale EIT waves discovered by Thompson et al. (1998) are the result of propagating fast magnetosonic waves (Wang 2000; Murawski, Nakariakov & Pelinovsky 2001; Ofman & Thompson 2002).

Recent observations by the Coronal Multichannel Polarimeter (CoMP) instrument (Tomczyk et al. 2007) and *TRACE* (see the overview by De Moortel & Rosner 2007) clearly indicate that coronal oscillations are ubiquitous and have amplitudes that peak at the p-mode frequency band. In the high corona, the CoMP instrument detects strong fluctuations of the line-of-sight Doppler velocity with a broad peak at 3.5 mHz. Correspondingly weak intensity oscillations are seen at the same frequency. This indicates that the observed waves are nearly incompressive, and as such Tomczyk et al. (2007) identified the waves as Alfvénic. However, in a low-β plasma, fast magnetosonic tube waves or kink waves are also nearly incompressive. Therefore, we posit that these observations in the high corona may also be fast kink waves.

On the other hand, the loop oscillations observed by *TRACE* have been identified as slow waves (e.g., Berghmans & Clette 1999; De Moortel, Ireland & Walsh 2000; De Moortel, Hood & Ireland 2002). The oscillations associated with sunspot loops have peak power at a period of 3 minutes (or a frequency of 5.5 mHz), while loops not associated with sunspots have peak power at a period of 5 minutes (or 3.3 mHz; De Moortel et al. 2002; Centeno, Collados & Trujillo Bueno 2006). Therefore, both slow and fast waves with frequencies associated with p-mode oscillations have been observed. The p modes, and possibly solar granulation, are clearly implicated as the ultimate source of many coronal fluctuations. In this paper, we concentrate on p modes as the driving mechanism.

If p modes are in fact responsible, the p modes must somehow manage to leak into the upper atmosphere, despite the fact that they become evanescent above the photosphere. Some have suggested that the leakage is accomplished by a "ramp effect," by which an inclined magnetic field effectively reduces the acoustic cutoff frequency of the atmosphere (De Pontieu, Erdélyi & De Moortel 2005; Hansteen et al. 2006; McIntosh & Jefferies 2006; Jefferies et al. 2006). However, we point out that the cutoff frequency for both the slow sausage wave and the fast kink wave can fall below the nonmagnetic acoustic cutoff frequency (see Roberts & Webb [1978] and Musielak & Ulmschneider [2001] for a derivation of the cutoff for sausage and kink waves, respectively). Therefore, a flux tube can act as a waveguide (Roberts 1981), permitting efficient penetration of the acoustic barrier presented by the photosphere. It may be possible that vertically aligned flux tubes are capable of carrying a sufficient flux of tube waves into the atmosphere to explain the observations.

We suggest the following mechanism. Within the solar convection zone, p-mode oscillations buffet the many magnetic fibrils that thread through the photosphere into the chromosphere and corona. This buffeting excites both sausage and kink waves on the fibrils, which then propagate both up and down the vertical field

lines. Those waves that travel downward are lost in the convection zone, whereas those that propagate upward pass through the photosphere into the upper atmosphere, where they manifest as coronal-loop oscillations and upward-propagating waves.

In this paper we estimate, by a semianalytic method, the atmospheric energy flux of sausage and kink waves that can be generated by this mechanism. Our calculation is a direct extension of the work by Bogdan et al. (1996), hereafter referred to as BHCC96. We demonstrate that f and p modes efficiently generate tube waves and that an energy flux in excess of 10^5 ergs cm^{-2} s^{-1} can be driven upward through photospheric levels. Whether, such a flux can survive passage through the chromosphere and transition region into the corona is left to subsequent work.

The paper is organized as follows. In §2 we describe the stationary configuration of the flux tubes and the equilibrium atmosphere in which they are embedded. §3 details the p-mode oscillations, and §4 derives the driven oscillations of the thin flux tubes. In §5 we present our primary results, the energy flux of tube waves and the damping rates of the p modes that those fluxes engender. §6 provides a discussion of our findings, where we compare our derived atmospheric energy fluxes with those obtained by observations.

2. The Equilibrium

We examine the excitation of waves on a thin magnetic fibril through the buffeting of the tube by acoustic oscillations within the solar convection zone. The fibril threads through a field-free atmosphere, and its axis is aligned with the force of gravity. We assume that in the absence of the acoustic wave field, the fibril and surrounding atmosphere are static and in equilibrium. In the following two subsections we describe the field-free atmosphere in which the fibril is embedded and the equilibrium configuration and structure of the fibril itself.

2.1. The Atmosphere

We restrict our attention to acoustic waves with wavelengths much shorter than the radius of the Sun; therefore, we may ignore the curvature of the solar surface. This allows us to make the simplifying assumption that the atmosphere is plane-parallel with constant gravity pointing downward, $\boldsymbol{g} = -g\hat{\boldsymbol{z}}$. The height coordinate z is defined to increase upward. We model the solar convection zone with an isentropically stratified atmosphere that is excised above a height $z = -z_0$, known as the truncation height. Below this height, $z < -z_0$, the atmosphere is polytropic and the gas pressure, mass density, and sound speed are power-law functions of height,

$$\rho_{\rm e}(z) = \rho_0 \left(-\frac{z}{z_0}\right)^m, \tag{2.1}$$

$$P_{\rm e}(z) = \frac{g z_0 \rho_0}{m+1} \left(-\frac{z}{z_0}\right)^{m+1} = P_0 \left(-\frac{z}{z_0}\right)^{m+1}, \tag{2.2}$$

$$c_{\rm e}^2(z) = -\frac{gz}{m}. \tag{2.3}$$

In the preceding equations, the subscript "e" is used to denote the nonmagnetic atmosphere that is "external" to the magnetic fibril. The constants ρ_0 and P_0 are the surface values of the mass density and gas pressure.

The constant m is the polytropic index, which has a special value that depends on the ratio of specific heats γ, because the atmosphere is isentropically stratified, $m = 1/(\gamma - 1)$.

An extremely diffuse and hot gas exists above the truncation height. For this work, we adopt the limiting case of a vacuum ($\rho \to 0$) with infinite temperature ($T \to \infty$), such that the pressure remains finite. At the surface, where $z = -z_0$, the pressure of this "hot corona" matches the pressure of the lower atmosphere (the model convection zone).

Following BHCC96, we specify the truncation depth z_0 and the surface mass density ρ_0 (and therefore the surface pressure P_0) by matching the surface layer of our model, $z = -z_0$, with the $\tau_{5000} = 1$ level of a solar model by Maltby et al. (1986). At this layer in the solar model $g = 2.775 \times 10^4$ cm s^{-1}, $\rho_0 = 2.78 \times 10^{-7}$ g cm^{-3}, and $P_0 = 1.21 \times 10^5$ g cm^{-1} s^{-1}. We adopt $m = 1.5$ (appropriate for $\gamma = 5/3$), which is a reasonable approximation to the bulk of the convection zone. With this choice of polytropic index, the truncation depth and surface sound speed become 392 km and 8.52 km s^{-1}, respectively.

2.2. The Magnetic Fibril

For simplicity, we assume that the magnetic fibril threading the truncated polytrope obeys the following properties:

1. The flux tube is straight, untwisted and axisymmetric.
2. The tube has a circular cross section.
3. The tube is vertically aligned and coincident with the $\hat{\boldsymbol{z}}$-axis.
4. The tube has a potential magnetic field lacking internal currents.
5. The boundary of the flux tube is marked by a current sheet.
6. The tube is thin, meaning that its radius is significantly smaller than any scale length in the atmosphere, including the density scale height and the wavelength of incident acoustic waves.

The last of these assumptions bears some further discussion. A sufficiently thin flux tube is unable to support internal forces and structures beyond hydrostatic balance. Thus, the gas pressure imposed by the external medium at the flux tube boundary must be matched by a total pressure that is constant with radius across the tube. This same argument holds for temperature as well. The temperature inside and outside must be identical (as are the pressure scale heights), because any initial difference would be destroyed by thermal and radiative diffusion. Continuity of total pressure across the flux tube interface requires that the magnetic pressure also has the same scale height. Hence, the value of the plasma parameter $\beta = 8\pi P/B^2$ must be constant with height within the tube.

This simple statement of constant β within the tube is a strong constraint on the geometry of the flux tube. Since the gas pressure in the solar atmosphere decreases rapidly with height, the magnetic field strength within the tube also decreases rapidly, and the flux tube must flare dramatically near the surface. Thus, at some height in the atmosphere, the approximation that the tube is thin must break down. The magnetic field outside of sunspots is generally found in the form of small magnetic elements. For such elements, the flaring that occurs with height becomes important within the chromosphere where neighboring

flux elements begin to collide, thereby forming a magnetic canopy. The thin-flux-tube approximation cannot be applied consistently within the upper atmosphere. In this work, we circumvent this problem by truncating the atmosphere and only studying wave propagation in the region where the flux tube remains thin. As will be discussed more fully in §4.3, the details of the tube geometry and thermodynamic structure within the upper atmosphere can be mimicked by an appropriate choice of boundary condition at the surface, $z = -z_0$.

For thin flux tubes of the sort described above, radial variation of the field strength can be ignored and the flux tube is completely defined by its total magnetic flux Θ and the plasma β. The tube's internal gas pressure $P(z)$, mass density $\rho(z)$, axial field strength $B(z)$, and cross-sectional area $A(z)$ are given by the equations

$$P(z) = \frac{\beta}{\beta+1} P_{\rm e}(z), \tag{2.4}$$

$$\rho(z) = \frac{\beta}{\beta+1} \rho_{\rm e}(z), \tag{2.5}$$

$$\frac{B^2(z)}{8\pi} = \frac{1}{\beta+1} P_{\rm e}(z), \tag{2.6}$$

$$A(z) = \frac{\Theta}{B(z)} = \left(\frac{\beta+1}{8\pi P_{\rm e}(z)}\right)^{1/2} \Theta. \tag{2.7}$$

For a flux tube with $\beta = 1.0$ embedded in a $m = 1.5$ polytrope with a surface mass density of $\rho_0 = 2.78 \times 10^{-7}$ g cm^{-3}, the magnetic field strength at the surface, $z = -z_0$, is 1.2 kG.

3. The p-Mode Oscillations

The nonmagnetic atmosphere surrounding the magnetic fibril supports acoustic oscillations that are trapped in a wave guide just below the surface. The upper boundary reflects upward-propagating waves and the increasing sound speed with depth refracts downward-propagating waves back towards the surface. Since the atmosphere is isentropic, the acoustic modes of this waveguide—the f and p modes—have a particularly simple form and can be expressed using a displacement potential Φ,

$$\boldsymbol{\xi}_{\rm e} = \boldsymbol{\nabla}\Phi, \tag{3.1}$$

$$\delta P_{\rm e} = -\rho_{\rm e} \frac{\partial^2 \Phi}{\partial t^2}, \tag{3.2}$$

$$\delta \rho_{\rm e} = -\frac{\rho_{\rm e}}{c_{\rm e}^2} \frac{\partial^2 \Phi}{\partial t^2}. \tag{3.3}$$

The vector $\boldsymbol{\xi}_{\rm e}$ is the fluid displacement, $\delta P_{\rm e}$ is the perturbed gas pressure, $\delta \rho_{\rm e}$ is the perturbed mass density and $c_{\rm e}$ is the sound speed. Since the tube is thin, it is incapable of supporting a temperature differential with its surrounding; thus, the sound speed inside and outside the tube are the same function of height $c(z) = c_{\rm e}(z)$. We drop the subscript on $c_{\rm e}$ from here on.

3.1. Wave Equation

Equations (3.1)–(3.3) can be combined into a single partial differential equation for the displacement potential,

$$\frac{\partial^2 \Phi}{\partial t^2} = c^2 \nabla^2 \Phi - g \frac{\partial \Phi}{\partial z}. \tag{3.4}$$

Equation (3.4) supports plane-wave solutions of the form

$$\Phi(\mathbf{x}, t) = \mathcal{A} e^{-i\omega t} e^{ikx} Q(z), \tag{3.5}$$

where $\mathcal{A}$ is the complex wave amplitude, ω is the temporal frequency, k is the wavenumber, and $Q(z)$ is the vertical eigenfunction; $Q(z)$ is dimensionless and $\mathcal{A}$ has units of length squared. We have assumed without loss of generality that the acoustic wave propagates in only one horizontal direction, the x-direction. Direct substitution into equation (3.4) produces an ODE for the eigenfunction $Q(z)$,

$$\left\{ c^2 \frac{d^2}{dz^2} - g \frac{d}{dz} + \left(\omega^2 - k^2 c^2\right) \right\} Q(z) = 0. \tag{3.6}$$

This equation can be cast in a useful dimensionless form by the substitutions

$$\nu^2 \equiv \frac{m\omega^2 z_0}{g}, \qquad w \equiv -2kz, \qquad \lambda \equiv 2kz_0, \qquad \kappa \equiv \frac{\nu^2}{\lambda},$$

resulting in the equation

$$\left\{ \frac{d^2}{dw^2} + \frac{m}{w} \frac{d}{dw} + \left(\frac{\kappa}{w} - \frac{1}{4} \right) \right\} Q(w) = 0. \tag{3.7}$$

The two solutions to equation (3.7) involve Whittaker's functions $W_{\kappa,\mu}(w)$ and $M_{\kappa,\mu}(w)$ (see Abramowitz & Stegun 1964),

$$Q(w) = w^{-(\mu+1/2)} \begin{cases} W_{\kappa,\mu}(w) \\ M_{\kappa,\mu}(w) \end{cases}, \tag{3.8}$$

where $\mu = (m+1)/2$. Whittaker's W function vanishes as $w \to \infty$, but is poorly behaved at the origin $w = 0$, whereas Whittaker's M function is well behaved at the origin and diverges exponentially as $w \to \infty$.

3.2. p-Mode Boundary Conditions

As boundary conditions we require that the solution vanishes deep in the atmosphere as $w \to \infty$, and we require that the Lagrangian pressure perturbation vanishes at the free upper surface $z = -z_0$ (or equivalently, $w = \lambda = 2kz_0$). The first of these requirements makes Whittaker's M function unsuitable. The second of these boundary conditions places a restriction on the allowed values of κ (or equivalently λ). Therefore, for a

fixed value of the frequency, the eigenvalue $\kappa = \kappa_n$ is quantitized and satisfies the following set of equations, which simply restate that the Lagrangian pressure perturbation vanishes at the surface,

$$\left(\frac{d}{dw} + \frac{\kappa_n}{m}\right) Q_n(\lambda_n) = 0, \tag{3.9}$$

where,

$$Q_n(w) = w^{-(\mu+1/2)} W_{\kappa_n,\mu}(w). \tag{3.10}$$

After using recursion relations for Whittaker's W function (see Abramowitz & Stegun 1964), the last two equations can be reduced to

$$W_{\kappa_n,\mu+1}(\lambda_n) = 0. \tag{3.11}$$

The lowest order solution with $n = 0$ is the fundamental mode or f mode, whereas the higher overtones $n > 0$ correspond to the p modes.

3.3. Acoustic Mode Energy

The energy density of an acoustic wave propagating through an isentropic media is given by Bray & Loughhead (1974),

$$\mathcal{E} = \frac{1}{2}\rho_{\rm e} \left|\dot{\boldsymbol{\xi}}_{\rm e}\right|^2 + \frac{1}{2}\frac{\delta P_{\rm e}^2}{\rho_{\rm e} c^2}, \tag{3.12}$$

where the vector $\dot{\boldsymbol{\xi}}_{\rm e}$ is the partial derivative of $\boldsymbol{\xi}_{\rm e}$ with respect to time.

After taking temporal averages of equation (3.12), integrating over height, and multiplying by the surface area of the Sun, one finds the following expression for the energy contained in f- and p-mode oscillations,

$$E_n = 4\pi R_\odot^2 \frac{g\rho_0}{4m} \frac{\nu^4}{\lambda_n^m} \frac{\left|\mathcal{A}_n\right|^2}{z_0^2} \mathcal{N}_n, \tag{3.13}$$

$$\mathcal{N}_n \equiv \int_{\lambda_n}^{\infty} dw\, \frac{w^m}{\kappa_n} \left\{ \left(\frac{dQ_n(w)}{dw}\right)^2 + \left(\frac{\kappa_n}{w} + \frac{1}{4}\right) Q_n^2(w) \right\}. \tag{3.14}$$

4. Excitation of Tube Waves

The magnetic fibril is buffeted and driven by f-mode and p-mode waves within the convection zone. Magnetosonic oscillations of thin flux tubes have been examined in detail by many authors (Spruit 1981, 1984; Stix 1991; Ryutova & Priest 1993; Bogdan et al. 1996), and can be fully described by two types of waves: kink and sausage. Sausage waves are axisymmetric pressure pulses that produce displacements that are

primarily parallel to the magnetic field, $\xi_\parallel(z,t)$. Kink waves produce perpendicular displacements, $\xi_\perp(z,t)$, and magnetic tension and buoyancy are the primary restoring forces.

4.1. Thin-Flux-Tube Equations

The sausage waves and the kink waves are driven respectively by the overpressure and the transverse velocity imposed on the outer surface of the flux tube by incident acoustic waves. Using the formulation of BHCC96, the sausage and kink waves can be described by the equations

$$\left\{\frac{\partial^2}{\partial t^2} - c_{\rm T}^2\frac{\partial^2}{\partial z^2} + \frac{\gamma g}{2}\frac{c_{\rm T}^2}{c^2}\frac{\partial}{\partial z}\right\}\xi_\parallel = \frac{\rho_{\rm e}}{\rho}\frac{c_{\rm T}^2}{V_{\rm A}^2}\frac{\partial^3\Phi}{\partial z\partial t^2}, \tag{4.1}$$

$$\left\{\frac{\partial^2}{\partial t^2} - c_{\rm K}^2\frac{\partial^2}{\partial z^2} + \frac{\gamma g}{2}\frac{c_{\rm K}^2}{c^2}\frac{\partial}{\partial z}\right\}\xi_\perp = 2\frac{\rho_{\rm e}}{\rho}\frac{c_{\rm K}^2}{V_{\rm A}^2}\frac{\partial^3\Phi}{\partial x\partial t^2}, \tag{4.2}$$

where $V_{\rm A}$ is the Alfvén speed, $c_{\rm T}$ is the cusp or tube speed, and $c_{\rm K}$ is the kink speed. This later speed is also referred to as the "mean" Alfvén speed, since it is the density-weighted mean of the Alfvén speeds inside and outside the tube:

$$V_{\rm A}^2 = \frac{B^2}{4\pi\rho}, \qquad c_{\rm T}^2 = \frac{c^2V_{\rm A}^2}{c^2+V_{\rm A}^2}, \qquad c_{\rm K}^2 = \frac{B^2}{4\pi(\rho+\rho_{\rm e})}.$$

Equations (4.1) and (4.2) describe the forced oscillations of sausage and kink waves on a slender tube. Clearly, in the limit of low β, the sausage waves are simply slow magnetosonic waves propagating along the thin tube (see Roberts & Webb [1978] for a derivation in an atmosphere with generic stratification). In this same limit, the kink waves are fast magnetosonic waves, with an enhanced effective density due to the fact that transverse motions of the tube must push and pull external fluid. However, in the parameter regime that corresponds to photospheric magnetic elements, the plasma β is roughly unity and the distinction of fast versus slow magnetosonic waves proves less useful. In any event, the sausage wave is primarily a pressure wave, whereas the kink wave is principally a tension wave.

The shaking of the fibril by p-mode oscillations appears as the forcing on the right-hand sides of equations (4.1) and (4.2) where the pressure perturbation and horizontal displacement have been replaced by appropriate derivatives of the displacement potential. The forcing for the sausage waves arises from the requirement that the total pressure is continuous across the tube boundary. The kink waves are driven by horizontal motions of the external media.

These equations have similar form and can be written compactly using the notation,

$$\left\{\frac{d^2}{ds^2} + \frac{\mu+1}{s}\frac{d}{ds} + \frac{\nu^2\epsilon_\sigma}{s}\right\}\xi_\sigma = \frac{\mathcal{A}_n}{z_0}f_\sigma(s), \tag{4.3}$$

where $s=-z/z_0$ is a dimensionless depth and σ represents either $\parallel$ or $\perp$, corresponding to the sausage and kink waves, respectively. The quantity ϵ_σ takes on the two values,

$$\epsilon_\parallel = \frac{2m+\beta(m+1)}{2m}, \qquad \epsilon_\perp = \frac{(m+1)(2\beta+1)}{2m}.$$

The forcing function $f_\sigma(s)$ depends on whether we are driving kink or sausage waves,

$$f_\parallel(s) \equiv -\frac{(m+1)(\beta+1)}{2m}\frac{\nu^2}{s}\frac{dQ_n(s)}{ds}, \tag{4.4}$$

$$f_\perp(s) \equiv i\frac{(m+1)(\beta+1)}{2m}\frac{\lambda_n\nu^2}{s}Q_n(s). \tag{4.5}$$

The homogeneous solutions to equation (4.3) can be expressed in terms of Hankel functions,

$$\psi_\sigma(s) = s^{-\mu/2}H_\mu^{(1)}\left(2\nu\sqrt{\epsilon_\sigma s}\right), \tag{4.6}$$

$$\theta_\sigma(s) = s^{-\mu/2}H_\mu^{(2)}\left(2\nu\sqrt{\epsilon_\sigma s}\right) = \psi_\sigma^*(s). \tag{4.7}$$

For the chosen time dependence (see eq. [3.5]), the ψ_σ solution represents a downward-propagating wave, while the θ_σ solution is an upward-propagating wave. Note that the two solutions are simply complex conjugates of each other, thus allowing all further equations to be expressed using solely ψ_σ.

The solution to the driven problem is constructed from the homogeneous solutions using a Green's function formulation,

$$\xi_\sigma(s) = -\frac{i\pi}{2}\frac{\mathcal{A}_n}{z_0}\left\{\psi_\sigma(s)\left[\Omega_\sigma + \int_1^s dr\; r^{\mu+1}\psi_\sigma^*(r)f_\sigma(r)\right] + \theta_\sigma(s)\int_s^\infty dr\; r^{\mu+1}\psi_\sigma(r)f_\sigma(r)\right\}. \tag{4.8}$$

This solution was constructed to satisfy specific boundary conditions. Deep in the atmosphere, as $s \to \infty$ (or $z \to -\infty$), ξ_σ becomes proportional to ψ_σ, thereby satisfying a causal radiation condition. At the surface $s = 1$ (or $z = -z_0$), the solution is a mixture of upward- and downward-propagating waves. The exact proportion of ψ_σ to θ_σ in this mixture is completely specified by the boundary-condition parameter Ω_σ. The boundary condition represents both the reflection that occurs directly at the upper surface and the combined effect of the entire upper atmosphere $z > -z_0$, which is not included explicitly in the calculation. Any physical choice of boundary condition can be satisfied by an appropriate value of Ω_σ. For example, $\Omega_\sigma = 0$ enforces a radiation condition, where only the upward-propagating wave is present at the surface.

The integrals that appear in equation (4.8) form the basis for all of the derived quantities that appear later. The p-mode eigenfunctions Q_n are purely real functions, and therefore the driving functions f_σ are either purely real (for the sausage) or purely imaginary (for the kink). This allows us to express both integrals compactly for both the sausage mode and the kink mode,

$$\mathcal{J}_\sigma(s) \equiv \int_1^s dr\; r^{\mu+1}\psi_\sigma(r)f_\sigma(r), \tag{4.9}$$

$$\mathcal{I}_\sigma \equiv \lim_{s\to\infty}\mathcal{J}_\sigma(s) = \int_1^\infty dr\; r^{\mu+1}\psi_\sigma(r)f_\sigma(r), \tag{4.10}$$

$$\mathcal{I}_\sigma - \mathcal{J}_\sigma(s) = \int_s^\infty dr\; r^{\mu+1}\psi_\sigma(r)f_\sigma(r). \tag{4.11}$$

We call $\mathcal{I}_\sigma$ the interaction integral between the p mode and the respective tube wave. Using these definitions explicitly, the displacements for the two types of waves take on the forms

$$\xi_\parallel(s) = -\frac{i\pi}{2}\frac{\mathcal{A}_n}{z_0}\left\{\psi_\parallel(s)\Big[\Omega_\parallel + \mathcal{J}^*_\parallel(s)\Big] + \psi^*_\parallel(s)\Big[\mathcal{I}_\parallel - \mathcal{J}_\parallel(s)\Big]\right\}, \tag{4.12}$$

$$\xi_\perp(s) = -\frac{i\pi}{2}\frac{\mathcal{A}_n}{z_0}\left\{\psi_\perp(s)\Big[\Omega_\perp - \mathcal{J}^*_\perp(s)\Big] + \psi^*_\perp(s)\Big[\mathcal{I}_\perp - \mathcal{J}_\perp(s)\Big]\right\}. \tag{4.13}$$

Note the difference in sign in front of $\mathcal{J}^*_\sigma$ in the first term in the curly braces. This difference arises because $f_\parallel$ is purely real and $f_\perp$ is purely imaginary.

In equations (4.12) and (4.13) the term $\psi_\sigma \mathcal{J}^*_\sigma$ represents the upward-propagating wave generated by the driver, while the term $\psi^*_\sigma\left[\mathcal{I}_\sigma - \mathcal{J}_\sigma\right]$ represents the downward wave directly generated by the driver. The term $\psi_\sigma\Omega_\sigma$ is a downward-propagating wave arising from reflection off the upper surface, plus any waves propagating downward from the upper atmosphere through the upper surface (perhaps caused by a reflection in the chromosphere or corona).

Note that the energy flux of waves generated by the driver and propagating away from the driving region is the same both upward and downward. This can be seen by examining only those terms in equations (4.12) and (4.13) that represent wave components directly generated by the driver. The downward component is evaluated as $s \to \infty$, and the upward component at $s = 1$,

$$\xi^{(\mathrm{down})}_\sigma = \mp\frac{i\pi}{2}\frac{\mathcal{A}_n}{z_0}\psi_\sigma\mathcal{I}^*_\sigma, \tag{4.14}$$

$$\xi^{(\mathrm{up})}_\sigma = -\frac{i\pi}{2}\frac{\mathcal{A}_n}{z_0}\psi^*_\sigma\mathcal{I}_\sigma. \tag{4.15}$$

This is a useful fact that will be exploited later.

4.2. Energy Flux of Tube Waves

At any point along the tube, the energy flux is given by the following expression (Bray & Loughhead 1974),

$$\boldsymbol{F} = \left(\delta P + \frac{\delta\boldsymbol{B}\cdot\boldsymbol{B}}{4\pi}\right)\dot{\boldsymbol{\xi}} - \frac{\delta\boldsymbol{B}\cdot\dot{\boldsymbol{\xi}}}{4\pi}\boldsymbol{B}. \tag{4.16}$$

The perturbed magnetic field for sausage waves is given by equation (A8) in Appendix A of BHCC96. The perturbed field for the kink waves can be derived directly from the induction equation of MHD,

$$\frac{\delta B_\parallel B}{4\pi} = \frac{2}{2+\gamma\beta}\delta P_\mathrm{e} + \frac{\gamma\beta}{2+\gamma\beta}\frac{B^2}{4\pi}\frac{\partial\xi_\parallel}{\partial z} - g\left(\rho - \frac{\gamma\beta}{2+\gamma\beta}\rho_\mathrm{e}\right)\xi_\parallel, \tag{4.17}$$

$$\delta B_\perp = B\frac{\partial\xi_\perp}{\partial z}. \tag{4.18}$$

Direct substitution of equations (4.12), (4.13), (4.17) and (4.18) into equation (4.16) produces the following vertical energy fluxes at the two boundaries. As $s \to \infty$,

$$F_{\parallel} = -\frac{\gamma\beta}{2+\gamma\beta}\frac{\pi g\rho_0\omega}{4(m+1)(\beta+1)}\frac{|\mathcal{A}_n|^2}{z_0^2}\left|\Omega_{\parallel}+\mathcal{I}_{\parallel}^*\right|^2 s^{\mu+1}, \tag{4.19}$$

$$F_{\perp} = -\frac{\pi g\rho_0\omega}{4(m+1)(\beta+1)}\frac{|\mathcal{A}_n|^2}{z_0^2}\left|\Omega_{\perp}-\mathcal{I}_{\perp}^*\right|^2 s^{\mu+1}, \tag{4.20}$$

and at $s = 1$,

$$F_{\parallel} = \frac{\gamma\beta}{2+\gamma\beta}\frac{\pi g\rho_0\omega}{4(m+1)(\beta+1)}\frac{|\mathcal{A}_n|^2}{z_0^2}\left(\left|\mathcal{I}_{\parallel}\right|^2-\left|\Omega_{\parallel}\right|^2+\mathcal{S}\right), \tag{4.21}$$

$$F_{\perp} = \frac{\pi g\rho_0\omega}{4(m+1)(\beta+1)}\frac{|\mathcal{A}_n|^2}{z_0^2}\left(|\mathcal{I}_{\perp}|^2-|\Omega_{\perp}|^2\right), \tag{4.22}$$

where,

$$\mathcal{S} = -\frac{(m+1)(\beta+1)}{2m}\nu^2\mathcal{Q}_n\left\{H_{\mu}^{(1)}\left(2\nu\sqrt{\epsilon_{\parallel}}\right)\left[\Omega_{\parallel}+\mathcal{I}_{\parallel}^*\right]+H_{\mu}^{(2)}\left(2\nu\sqrt{\epsilon_{\parallel}}\right)\left[\Omega_{\parallel}^*+\mathcal{I}_{\parallel}\right]\right\}, \tag{4.23}$$

$$\mathcal{Q}_n = Q_n(s=1) = Q_n(w=\lambda_n). \tag{4.24}$$

Note that the flux passing both down and up the tube are functions of the boundary condition that is applied at the surface $s = 1$ through the Ω_σ parameter. Furthermore, the sausage mode also possesses a term $\mathcal{S}$ in the energy flux at the upper surface $s = 1$ which arises because the driver, equation (4.4), does not vanish at the surface. This term is essentially the p-mode eigenfunction multiplied by the real part of the vertical displacement within the tube. Depending on the phasing between these two quantities, this surface driving term can take on positive or negative values.

Furthermore, the flux deep in the atmosphere $s \to \infty$ increases with depth $F \sim s^{\mu+1}$, but it does so at the same rate that the cross-sectional area of the tube decreases,

$$\begin{aligned} A(s) &= \left(\frac{(m+1)(\beta+1)}{8\pi g z_0\rho_0}\right)^{1/2}\Theta\, s^{-(\mu+1)}, \\ &= A_{\rm s}\, s^{-(\mu+1)}. \end{aligned} \tag{4.25}$$

Therefore, below those layers in which p modes drive waves, the rate at which energy passes down the tube is constant with depth,

$$\dot{E}_{\parallel} = -\frac{\gamma\beta}{2+\gamma\beta}\frac{\pi g\rho_0\omega A_{\rm s}}{4(m+1)(\beta+1)}\frac{|\mathcal{A}_n|^2}{z_0^2}\left|\Omega_{\parallel}+\mathcal{I}_{\parallel}^*\right|^2, \tag{4.26}$$

$$\dot{E}_\perp = -\frac{\pi g \rho_0 \omega A_\mathrm{s}}{4(m+1)(\beta+1)} \frac{|\mathcal{A}_n|^2}{z_0^2} \left| \Omega_\perp - \mathcal{I}_\perp^* \right|^2 . \tag{4.27}$$

In these two equations, $\dot{E}$ is negative for energy escaping the p-mode cavity, or in other words, if the energy flux is downward.

At the upper surface $s = 1$ a similar result is obtained,

$$\dot{E}_\parallel = -\frac{\gamma\beta}{2+\gamma\beta} \frac{\pi g \rho_0 \omega A_\mathrm{s}}{4(m+1)(\beta+1)} \frac{|\mathcal{A}_n|^2}{z_0^2} \left(\left| \mathcal{I}_\parallel \right|^2 - \left| \Omega_\parallel \right|^2 + \mathcal{S} \right), \tag{4.28}$$

$$\dot{E}_\perp = -\frac{\pi g \rho_0 \omega A_\mathrm{s}}{4(m+1)(\beta+1)} \frac{|\mathcal{A}_n|^2}{z_0^2} \left(\left| \mathcal{I}_\perp \right|^2 - \left| \Omega_\perp \right|^2 \right). \tag{4.29}$$

In these expressions, $\dot{E}$ is once again negative for energy escaping the p-mode cavity. However, in this case this requires that the flux is upward into the upper atmosphere above our model convection zone.

4.3. Boundary Conditions

We apply two different boundary conditions at the surface and track the results of each. The first boundary condition is the requirement that the stress vanishes at the upper surface $s = 1$. Of course, for this boundary condition, the energy flux through the upper surface must be identically zero. We include this boundary condition because it is the same boundary condition adopted by BHCC96. The second boundary condition that we apply maximizes the energy flux that passes up through the upper surface. This boundary condition allows us to compute an upper limit on the amount of tube-wave energy that is driven into the upper atmosphere.

4.3.1. Stress-Free Condition

For the sausage mode, the stress-free condition is enforced by requiring that the divergence of the displacement vector vanishes at the upper surface. This is equivalent to setting the Lagrangian pressure perturbation to zero. BHCC96 have shown that for the sausage waves,

$$\boldsymbol{\nabla} \cdot \boldsymbol{\xi} = \frac{\beta}{2+\gamma\beta} \frac{1}{P} \left(-\delta P_\mathrm{e} + \frac{B^2}{4\pi} \frac{d\xi_\parallel}{dz} + g\rho_\mathrm{e} \xi_\parallel \right). \tag{4.30}$$

After inserting δP_e and $\xi_\parallel$, and after substantial manipulation, one finds that $\boldsymbol{\nabla} \cdot \boldsymbol{\xi} = 0$ requires,

$$\Omega_\parallel = i \frac{(m+1)(\beta+1)}{m\pi} \nu^2 \frac{\mathcal{Q}_n}{\mathcal{H}_\parallel} - \frac{\mathcal{H}_\parallel^*}{\mathcal{H}_\parallel} \mathcal{I}_\parallel, \tag{4.31}$$

$$\mathcal{H}_\parallel \equiv \nu \sqrt{\epsilon_\parallel} H_{\mu+1}^{(1)} \left(2\nu\sqrt{\epsilon_\parallel} \right) + (\beta+1)(\mu+1) H_\mu^{(1)} \left(2\nu\sqrt{\epsilon_\parallel} \right). \tag{4.32}$$

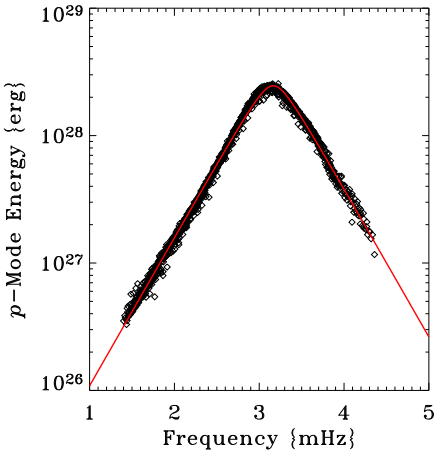

Fig. 1.— Energy contained in solar p modes with harmonic degrees in the range $3 < \ell \leq 150$ and orders $n > 0$. Diamonds indicate the measurements of Komm, Howe & Hill (2003). As can be clearly seen, the energy is primarily a function of frequency. The solid red curve is a maximum-likelihood fit to the data using the functional form appearing in eq. (5.3).

For the kink waves, BHCC96 imposed the boundary condition at $s = 1$ that the magnetic tension force vanishes or equivalently, that the second derivative of the displacement with respect to height vanishes. We do not follow their example, for the simple reason that the horizontal force equation for the kink mode possesses two other terms, the buoyancy force and the external p-mode forcing. In equation (4.2) the term with the second derivative with respect to height arises from the magnetic tension, while the term on the left-hand side with the single derivative with respect to height is the buoyancy force. The external forcing is the right-hand side of the equation. Neither the buoyancy nor external forcing vanish when the tension force is zero. However, setting the displacement itself to zero at the surface is sufficient to specify a net horizontal force of zero. Therefore, this is the proper stress-free boundary condition that we apply. Evaluation of equation (4.13) at $s = 1$ reveals that this stress-free boundary condition requires

$$\Omega_\perp = -\frac{H_\mu^{(2)}\left(2\nu\sqrt{\epsilon_\perp}\right)}{H_\mu^{(1)}\left(2\nu\sqrt{\epsilon_\perp}\right)}\mathcal{I}_\perp. \tag{4.33}$$

Direct substitution of the values of Ω_σ given by equations (4.31) and (4.33) into the relevant energy-transfer rates, equations (4.28) and (4.29), reveal that the energy flux through the upper surface is zero, as expected.

4.3.2. Maximal-Flux Condition

The maximal-flux boundary condition allows us to place an upper limit on the energy contained within coronal-loop waves that are generated by p-mode forcing in the solar convection zone. We specify the value of Ω_σ by maximizing the energy flux shown in equations (4.21) and (4.22),

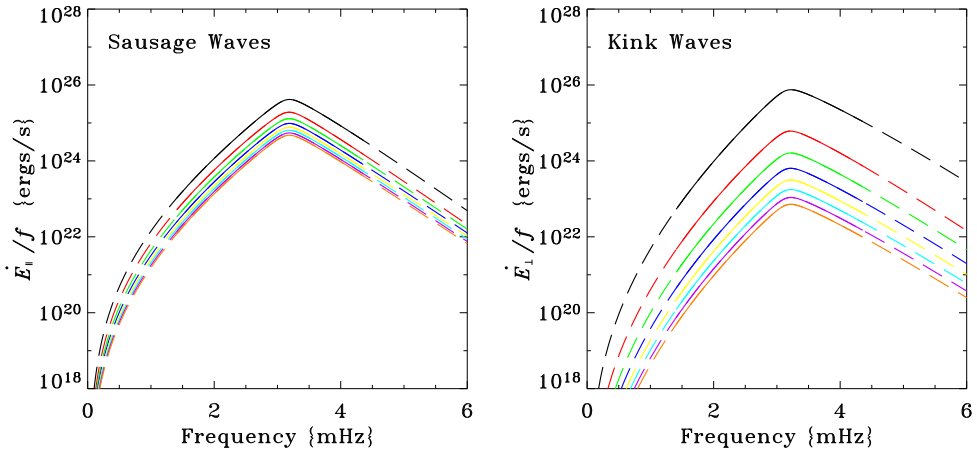

Fig. 2.— Energy flux of tube waves driven up through the model photosphere. The solar surface is peppered with identical thin flux tubes with $\beta = 1.0$ and a combined filling factor f. The fluxes shown are divided by this filling factor. The different curves correspond to the flux driven by different order p modes: f (*black*), p_1 (*red*), p_2 (*green*), p_3 (*dark blue*), p_4 (*yellow*), p_5 (*aqua*), p_6 (*violet*), and p_7 (*orange*). The range of frequencies for which the curves are solid corresponds to the window where Komm, Howe & Hill (2003) measured p-mode energies. Frequencies where the curves are dashed indicate extrapolations of the measured p-mode energy. These curves are for the case where a maximal-flux boundary condition has been applied at the photosphere.

$$\Omega_\parallel = -\frac{(m+1)(\beta+1)}{2m}\nu^2 \mathcal{Q}_n H_\mu^{(2)}\left(2\nu\sqrt{\epsilon_\parallel}\right), \tag{4.34}$$

$$\Omega_\perp = 0. \tag{4.35}$$

These values for Ω_σ are the only extrema in F_σ, and a simple check confirms that the upward fluxes are maximized at these values. Furthermore, the flux through the upper surface is identical to the downward flux for this boundary condition.

One might assume that the maximal-flux boundary condition is equivalent to applying a radiation condition at $s = 1$. However, this is only true for the kink wave. A radiating upper boundary requires that $\Omega_\sigma = 0$. If the p-mode eigenfunction vanished at the upper surface, the maximal-flux condition would indeed be $\Omega_\parallel = 0$. The fact that the driver is nonzero at the surface ensures that the radiation condition and maximal-flux condition are different requirements.

5. Results

In the following two subsections we examine several properties obtained from the energy fluxes derived in §4.2. In particular, in §5.1 we present the energy flux of tube waves driven into the upper atmosphere by the p-mode driving. In §5.2 we examine the damping imposed on the p modes themselves by the excitation of tube waves.

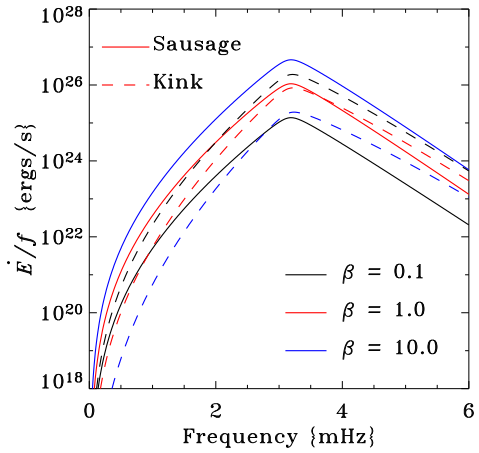

Fig. 3.— Energy flux of tube waves driven up through the model photosphere summed over all mode orders $n < 8$. The different colors correspond to models with flux tubes with different values of β: $\beta = 0.1$ (*black*), $\beta = 1.0$ (*red*), and $\beta = 10.0$ (*blue*).

An examination of the energy-loss rates, equations (4.26)–(4.29), reveal that all can be computed directly from the p-mode eigenfunctions $Q_n(w)$, the eigenvalues $\kappa_n(\nu)$, the mode-energy integral $\mathcal{N}_n$, and the interaction integrals $\mathcal{I}_\parallel$ and $\mathcal{I}_\perp$. We compute all of these quantities using a shooting technique with adaptive-step-size fifth-order Runge-Kutta integration. The eigenproblem is solved iteratively at each dimensionless frequency ν and for all mode orders $n < 8$. Subsequently, once the eigenfunction and eigenvalue have been established, all integrals ($\mathcal{N}_n$, $\mathcal{I}_\parallel$, and $\mathcal{I}_\perp$) are computed during the final iteration of the numerical integrator.

5.1. Atmospheric Fluxes of Tube Waves

In §4.2 we derived, for a single flux tube, the energy flux of tube waves that passes through the upper surface into the upper atmosphere. Since we are interested in comparing the derived fluxes with energy fluxes observed within the chromosphere or corona, the energy flux produced by a single flux tube is not of particular relevance. Instead, we need the energy flux produced collectively by all of the flux tubes that might contribute to the observations. It is easiest and most direct if we examine the aggregate behavior of the entire Sun. The total rate of energy deposition $\dot{E}_\sigma^{\rm tot}$ is simply the deposition rate for a single tube $\dot{E}_\sigma$ multiplied by the number of tubes on the solar surface N. If we assume that all of the flux tubes that pierce the photosphere are identical (with the same value of β, magnetic flux Θ, etc.) then the number of flux tubes depends only on the surface cross-sectional area of a single tube $A_{\rm s}$ and the filling factor f. Using $N = 4\pi R_\odot^2 f / A_{\rm s}$ and equations (4.28)–(4.29), one finds

$$\dot{E}_\parallel^{\rm tot} = -\frac{\gamma\beta}{2+\gamma\beta}\frac{\pi^2 g\rho_0\omega f R_\odot^2}{(m+1)(\beta+1)}\frac{|\mathcal{A}_n|^2}{z_0^2}\left(\left|\mathcal{I}_\parallel\right|^2 - \left|\Omega_\parallel\right|^2 + \mathcal{S}\right), \tag{5.1}$$

$$\dot{E}_\perp^{\rm tot} = -\frac{\pi^2 g\rho_0\omega f R_\odot^2}{(m+1)(\beta+1)}\frac{|\mathcal{A}_n|^2}{z_0^2}\left(\left|\mathcal{I}_\perp\right|^2 - \left|\Omega_\perp\right|^2\right). \tag{5.2}$$

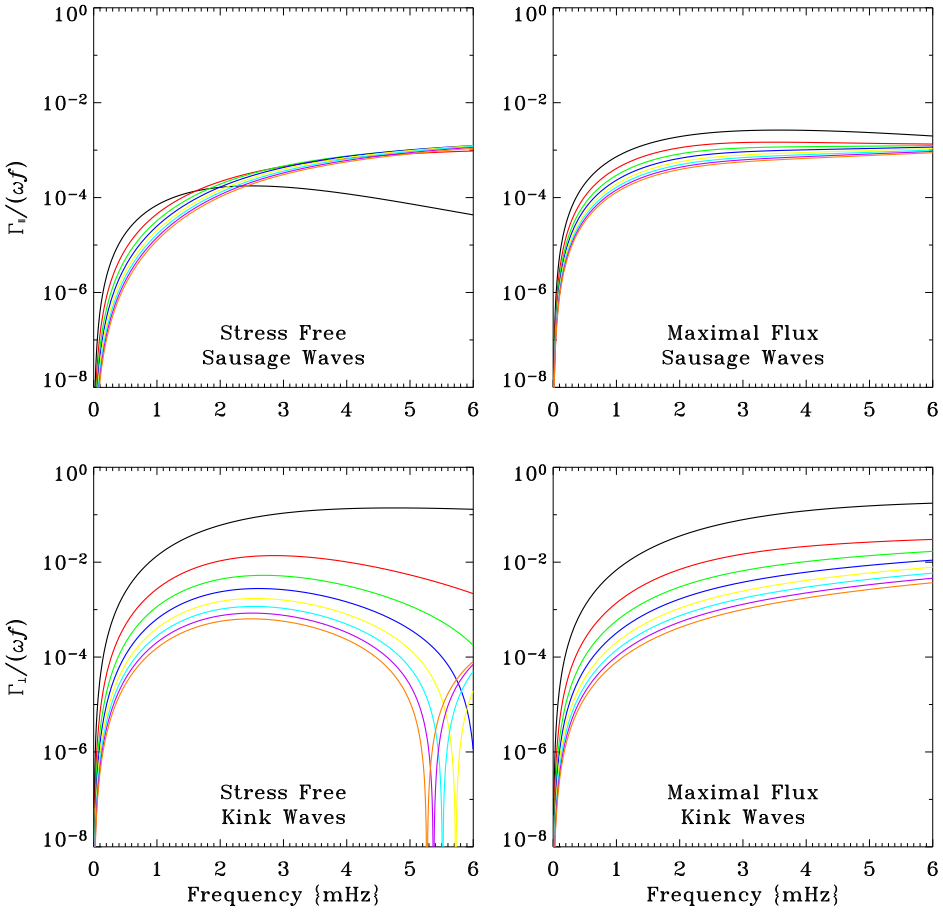

Fig. 4.— Damping rate of f and p modes caused by the excitation of both sausage and kink waves on thin magnetic flux tubes. The tubes have $\beta = 0.1$. Two different photospheric boundary conditions are applied: stress free and maximal flux. The nulls in the damping rate seen between 5 and 6 mHz for the kink wave under the stress-free boundary condition arise because the downward-propagating wave and the wave that reflects off the upper surface destructively interfere.

The final step required to convert these equations into a physically meaningful graph is specification of the amplitudes $\mathcal{A}_n$ of the incident p modes. We use measured p-mode energies to accomplish this. Figure 1 shows p-mode energies for harmonic degrees between 4 and 150 as measured by Komm, Howe & Hill (2003). The energies are largely a function of frequency alone and reach a peak value of roughly 2.5×10^{28} ergs at a frequency of 3.2 mHz. To either side of this peak the energy falls off exponentially with frequency. In order to extrapolate to frequencies outside the observed range, we fit these energies with a curve of the form

$$E_{\rm fit}(\eta) = a \exp\left(-\frac{\sqrt{(\eta-\eta_0)^2+\delta^2}}{d}\right). \tag{5.3}$$

In this equation, η is the cyclic p-mode frequency, a is an amplitude, η_0 is the frequency of peak energy, d is a wing decay rate, and δ is a core width. Using a maximum-likelihood procedure we find $a = 3.71 \times 10^{28}$ ergs, $\eta_0 = 3.16$ mHz, $\delta = 0.152$ mHz, and $d = 0.372$ mHz. This fit is shown in Figure 1 with the red curve. With this fit we can estimate the p-mode amplitudes $\mathcal{A}_n$ by equating the mode energies in equation (3.13) with the fit,

$$|\mathcal{A}_n|^2 = \frac{m\lambda_n^m}{\nu^4}\frac{z_0^2}{\pi R_\odot^2}\frac{E_{\rm fit}}{g\rho_0\mathcal{N}_n}. \tag{5.4}$$

With this final ingredient we can evaluate the energy-deposition rates appearing in equations (5.1) and (5.2). These rates represent the amount of energy that is driven into the upper atmosphere in the form of sausage and kink waves. Figure 2 presents the resulting energy-deposition rates for $\beta = 1.0$. Figure 3 shows the rate summed over all p modes for three different values of β, representing weak ($\beta = 10$), intermediate ($\beta = 1.0$), and strong magnetic field ($\beta = 0.1$). A value of $\beta = 1.0$ is appropriate for small magnetic elements in the photosphere, corresponding to a surface magnetic field strength of 1.2 kG. The other values of β correspond to surface magnetic field strengths of 0.53 kG for $\beta = 10$ and 1.6 kG for $\beta = 0.1$. We have included the results for all three values of β to demonstrate the behavior as β changes. In particular, note that as the surface field strength decreases (β increases) the energy-transfer rate for kink waves decreases, whereas the rate for sausage waves increases. For all values of β the falloff at both high and low frequency is the result of the decrease in the measured p-mode energy spectrum (and hence amplitude $\mathcal{A}_n$) away from the peak at 3.2 mHz.

5.2. p-Mode Damping Rates

Since the tube waves carry away energy from the acoustic cavity, this energy must come from the p modes themselves, thereby damping the solar acoustic modes. We define a damping rate separately for the excitation of sausage and kink waves,

$$\Gamma_\sigma = -\frac{1}{2\pi}\frac{\dot{E}_\sigma}{E_n}. \tag{5.5}$$

Using the energy-deposition rates provided in equations (4.26)–(4.29), we compute the damping rates,

$$\frac{\Gamma_\parallel}{\omega} = \frac{\beta}{4(\beta+1)\epsilon_\parallel}\frac{A_{\rm s}}{4\pi R_\odot^2}\frac{\lambda_n^m}{\nu^4}\frac{\left|\Omega_\parallel + \mathcal{I}_\parallel^*\right|^2 + \left|\mathcal{I}_\parallel\right|^2 - \left|\Omega_\parallel\right|^2 + \mathcal{S}}{\mathcal{N}_n}, \tag{5.6}$$

$$\frac{\Gamma_\perp}{\omega} = \frac{1}{2\gamma(\beta+1)}\frac{A_{\rm s}}{4\pi R_\odot^2}\frac{\lambda_n^m}{\nu^4}\frac{\left|\Omega_\perp - \mathcal{I}_\perp^*\right|^2 + \left|\mathcal{I}_\perp\right|^2 - \left|\Omega_\perp\right|^2}{\mathcal{N}_n}. \tag{5.7}$$

In each of the expressions above, the first term in the numerator of the final fraction corresponds to energy lost down the tube, while the remaining terms in the numerator arise from energy lost through the upper surface. As stated previously, for the stress-free boundary condition the downward term is identically zero, and for the maximal-flux boundary condition the upward and downward terms are equal.

Figures 4–6 present these damping rates for three values of β. The most unusual feature within these graphs occurs for $\beta = 0.1$ in Figure 4. At a frequency around 5.5 mHz, the damping rate arising from the excitation of kink waves with the stress-free boundary has nulls where the damping drops to zero. Such nulls are to be expected. First, as previously noted, the upward direct wave and the downward direct wave generated by the driver possess the same energy flux. Second, the stress-free boundary reflects all upward-propagating wave energy back into the convection-zone model. These two facts lead one to the conclusion that the reflected wave and the downward direct wave have the same amplitude. There will be frequencies at which the phases of these two components are such that complete destructive interference occurs. At such a frequency, the damping rate will vanish because energy is driven neither up nor down the tube. A similar result was found by Crouch & Cally (1999).

6. Discussion

We have computed the energy flux of sausage and kink waves that are generated in the solar convection zone by the buffeting of magnetic fibrils by ambient f and p modes. We treat the fibrils as vertically-aligned thin flux tubes. The tubes act as waveguides, much like a fiber-optic cable that ducts the propagation of light. Waves are generated locally within the p-mode cavity and freely propagate both up and down the tubes—one can easily verify that there are no turning points for our model's stratification. Those waves that propagate downward extract energy from the incident p mode and disappear into the convection zone. Those waves that propagate upward also damp the p mode and travel through the photosphere along the flux tube into the upper atmosphere. Such waves may well be the source of both coronal-loop oscillations and the ubiquitous waves observed throughout the corona.

6.1. Energy Flux of Tube Waves in the Upper Atmosphere

To determine if p-mode buffeting of small magnetic elements is a viable mechanism to explain the waves observed in the corona, we directly compare our derived wave fluxes with the observed fluxes. First, we comment that the spectral behavior of our derived energy fluxes is correct by construction. As stated previously, the shape of observed coronal wave spectra mimics spectra of p-mode energies—a broad peak at 3.5 mHz without resonances or nulls. Since our energy fluxes are directly proportional to the p-mode energy spectra, we clearly match this observed property well. Now, to determine whether the predicted amount of wave energy is reasonable. Table 1 provides the results of summing the tube-wave fluxes generated by all p modes with a frequency below 5 mHz. In different columns, we include both the energy flux (ergs cm^{-2} s^{-1}) and energy-transfer rate (ergs s^{-1}) for the entire solar surface.

Table 1: INTEGRATED ATMOSPHERIC ENERGY FLUX

β	$\dot{E}_{\parallel}/f$ {ergs s^{-1}}	$\dot{E}_{\parallel}/(4\pi R_{\odot}^2 f)$ {ergs cm^{-2} s^{-1}}	$\dot{E}_{\perp}/f$ {ergs s^{-1}}	$\dot{E}_{\perp}/(4\pi R_{\odot}^2 f)$ {ergs cm^{-2} s^{-1}}
0.10	3.81×10^{27}	6.25×10^{4}	1.01×10^{29}	1.65×10^{6}
1.00	3.54×10^{28}	5.82×10^{5}	5.41×10^{28}	8.88×10^{5}
10.0	1.84×10^{29}	3.02×10^{6}	1.35×10^{28}	2.22×10^{5}

The energy fluxes presented in Table 1 are quite significant. De Moortel & Rosner (2007) estimate that, depending on the mass density of coronal loops, the energy carried by loop oscillations is $\dot{E} \approx f_{\rm c} \times 3 \times (10^{25} -$

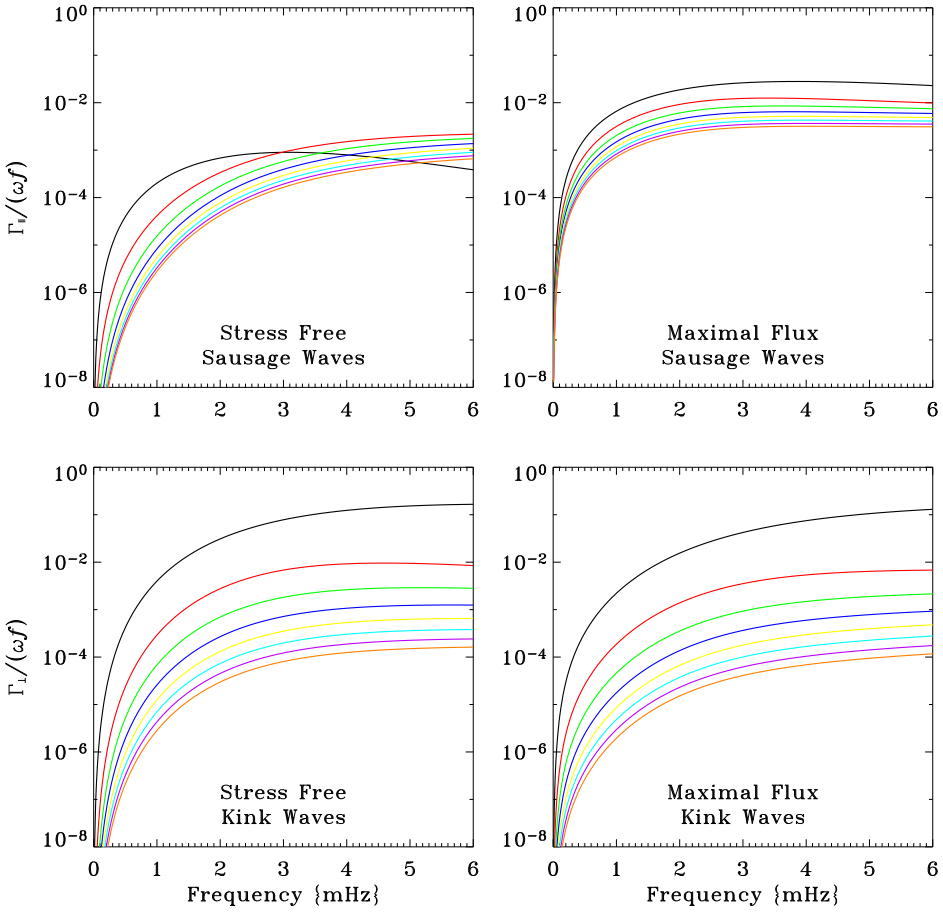

Fig. 5.— Same as Fig. 4, except that the thin flux tubes have $\beta = 1.0$.

10^{26}) ergs s^{-1}, where f_c is the coronal filling factor. Tomczyk et al. (2007) estimate that the upward energy flux of waves in the high corona is 10 ergs cm^{-2} s^{-1}, or $\dot{E} \approx 10^{24}$ ergs s^{-1} if multiplied by the solar surface area.

If we adopt a typical value of $\beta = 1.0$ for magnetic elements in the photosphere and a value of $f = 0.01$ for the photospheric filling factor, we find that our derived energy-transfer rates are 3.5×10^{26} ergs s^{-1} and 5.4×10^{26} ergs s^{-1} for the sausage and kink waves, respectively. While these numbers slightly exceed the estimates of De Moortel & Rosner (2007) and exceed the estimate of Tomczyk et al. (2007) by several orders of magnitude, we must keep in mind that our theoretically derived fluxes are the maximum possible flux that can be driven upward at the photospheric level. Reflection and absorption within the chromosphere and transition region are ignored. Clearly sufficient energy can be converted from p modes to tube waves to explain the observations; however, whether the attenuation of such waves allows them to reach high into the corona remains to be seen. We remind the reader that flux tubes can act as waveguides. The acoustic cutoff frequency of the nonmagnetized atmosphere is not the relevant quantity to determine whether the tube waves are propagating. Instead, the sausage and the kink waves have separate cutoff frequencies which

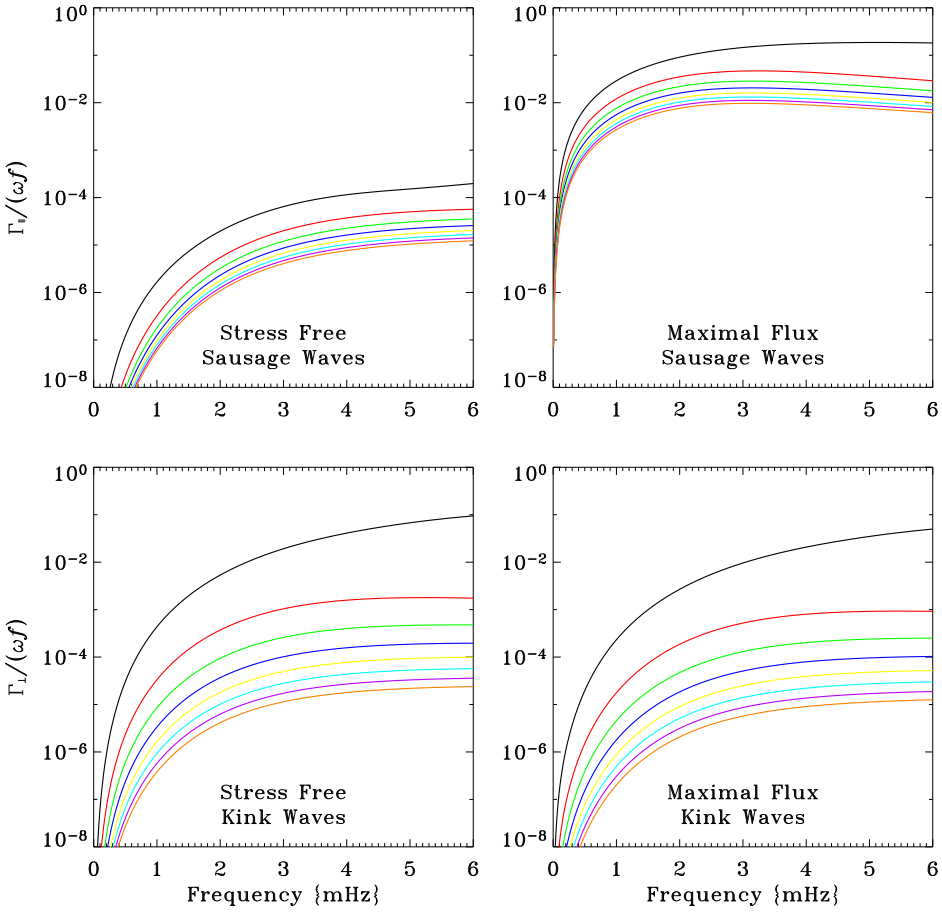

Fig. 6.— Same as Fig. 4, except that the thin flux tubes have $\beta = 10.0$.

can be lower than the acoustic cutoff of the surrounding media, depending on the properties of the tube (see Roberts & Webb 1978; Musielak & Ulmschneider 2001). Therefore, inclination of the field may not be required for magnetosonic waves to "tunnel" through the photosphere and temperature-minimum region.

6.2. Damping and p-Mode Line Widths

The excitation of tube waves extracts energy from the incident p mode that drives the oscillations. Figures 4–6 show the resulting damping rate. In order to determine whether these damping rates are significant, in Figure 7 we plot the damping rates for $\beta = 1.0$ and a filling factor of 0.01. We then overlay the p-mode full widths measured by Komm, Howe & Hill (2003). From this figure, one can see that the excitation of tube waves is likely to be a significant damping source only for the lowest order p modes. The damping is also a strong function of the boundary condition. The stress-free boundary produces significant damping only for the f mode, and most of the energy is converted into kink waves. For the maximal-flux boundary,

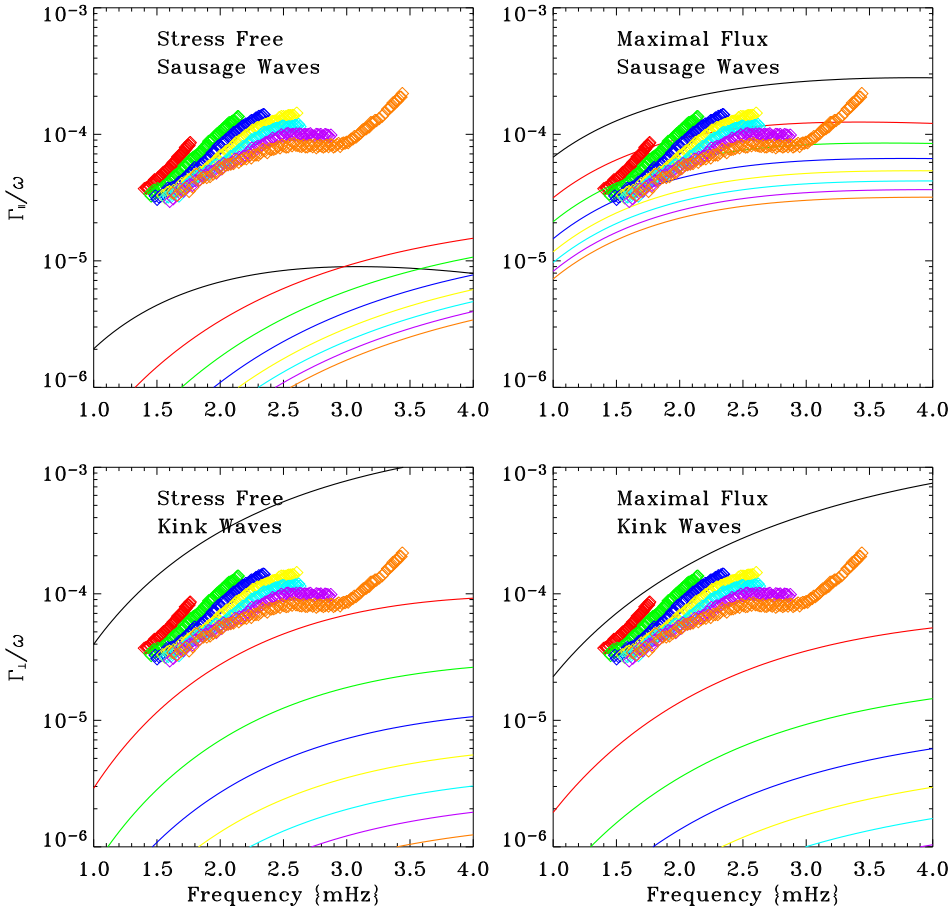

Fig. 7.— Same as Fig. 4, except that the value of β is 1.0 and measured full widths of the p modes have been overplotted with diamonds. Each mode order is plotted with a different color, using the same color scheme as in the theoretical curves: f (*black*), p_1 (*red*), etc. The full widths were measured by Komm, Howe & Hill (2003) and only orders 1–7 are shown.

markedly more energy is converted into sausage waves than kink waves, and the damping is important for $n < 5$.

6.3. Conclusions

We have demonstrated that p-mode buffeting of thin flux tubes can easily generate the flux and spectral dependence of waves observed in the corona, in the form of either longitudinal sausage waves or transverse kink waves. However, we only show that these large fluxes are possible at the photospheric level. Therefore, the remaining problem is one of transmission: Can the tube waves successfully propagate high into the corona without being absorbed or reflected at lower levels in the atmosphere? We plan in future efforts to include

a realistic model of the temperature minimum and low chromosphere, thereby accounting for the flaring of flux tubes with height and their eventual merger into a magnetic canopy. However, the semianalytic method used here is likely to prove of limited usefulness once the model atmosphere and model flux tubes become sufficiently complicated. Numerical simulations of the interaction between p modes and flux tubes will probably provide the ultimate answer. Such models have been previously built to investigate the absorption of acoustic waves by sunspots; however, these models have by explicit construction eliminated upward propagation of the resulting tube waves. The inclusion of a chromosphere and realistic upper boundary conditions is needed.

We thank Rudi Komm for providing data of p-mode energies and we thank D. Haber and G. Dickinson for help with the preparation of this manuscript. We are also indebted to the anonymous reviewer who made useful suggestions. B.W.H. acknowledges support from NASA and NSF through grants NAG5-12491, NAG5-13520, NNG05GM83G, NNX07AH82G and ATM-0219581. R.J. acknowledges discussions with V. Nakariakov and funding from Engineering and Physical Sciences Research Council, grant EP/C548795/1.

REFERENCES

Abramowitz, M., & Stegun, I. A. 1964, Handbook of Mathematical Functions, (New York: Dover Publications), 507

Aschwanden, M. J., Fletcher, L., Schrijver, C. J., & Alexander, D. 1999, ApJ, 520, 880

Berghmans, D. & Clette, F. 1999, Sol. Phys., 186, 207

Bogdan, T. J., Hindman, B. W., Cally, P. S., & Charbonneau, P. 1996, ApJ, 465, 406 (BHCC)

Bray, R. J., & Loughhead, R. E. 1974, The Solar Chromosphere (London: Chapman and Hall)

Centeno, R., Collados, M., & Trujillo Bueno, J. 2006, in ASP Conf. Ser. 358, Solar Polarization 4, ed. R. Casini & B. W. Lites (San Francisco: ASP), 465

Crouch, A. D., & Cally, P. S. 1999, ApJ, 521, 878

DeForest, C. E., & Gurman, J. B. 1998, ApJ, 501, L217

De Moortel, I., Hood, A. W., & Ireland, J. 2002, A&A, 381, 311

De Moortel, I., Ireland, J., Hood, A. W., & Walsh, R. W. 2002, A&A, 387, L13

De Moortel, I., Ireland, J., & Walsh, R. W. 2000, A&A, 355, 311

De Moortel, I., & Rosner, R. 2007, Sol. Phys., 246, 53

De Pontieu, B., Erdélyi, R., & De Moortel, I. 2005, ApJ, 624, L61

Hansteen, V. H., De Pontieu, B., Rouppe van der Voort, L., van Noort, M., Carlsson, M. 2006, ApJ, 647, L73

Jefferies, S. M., McIntosh, S. W., Armstrong, J. D., Bogdan, T. J., Cacciani, A., Fleck, B. 2006, ApJ, 648, L151

Komm, R., Howe, R., & Hill, F. 2003, in *Proc. of SoHO 12 / GONG+ 2002 Local and Global Helioseismology: The Present and Future*, (ESA SP–517), 325

Maltby, P., Avrett, E. H., Carlsson, M., Kjelsdeth-Moe, O., Kurucz, R. L., & Loeser, R. 1986, ApJ, 306, 284

Marsh, M. S., Walsh, R. W., De Moortel, I., & Ireland, J. 2003, A&A, 404, L37

McIntosh, S. W., & Jefferies, S. M. 2006, ApJ, 647, L77

Murawski, K., Nakariakov, V. M., & Pelinovsky, E. N. 2001, A&A, 366, 306

Musielak, Z. E., & Ulmschneider, P. 2001, A&A, 370, 541

Nakariakov, V. M., Ofman, L., DeLuca, E. E., Roberts, B., & Davila, J. M. 1999, Science, 285, 862

Ofman, L., Romoli, M., Poletto, G., Noci, G., & Kohl, J. L. 1997, ApJ, 491, L111

Ofman, L., Nakariakov, V. M., & DeForest, C. E. 1999, ApJ, 514, 441

Ofman, L., & Thompson, B. J. 2002, ApJ, 574, 440

Roberts, B. 1981, Sol. Phys., 69, 27

Roberts, B., & Webb, A. R. 1978, Sol. Phys., 56, 5

Ryutova, M. P., & Priest, E. R. 1993, ApJ, 419, 349

Spruit, H. C. 1981, A&A, 98, 155

Spruit, H. C. 1984, in Small Scale Dynamical Processes in Quiet Stellar Atmospheres, ed. S. L. Keil (Sunspot, NM: National Solar Observatory), 249

Stix, M. 1991, The Sun (Berlin: Springer)

Thompson, B. J., Plunkett, S. P., Gurman, J. B., Newmark, J. S., St. Cyr, O. C., & Michels D. J. 1998, Geophys. Res. Lett., 25, 2465

Tomczyk, S., McIntosh, S. W., Keil, S. L., Judge, P. G., Schad, T., Seeley, D. H., Edmondson, J. 2007, Science, 317, 1192

Verwichte, E., Nakariakov, V. M., Cooper, F. C. 2005, A&A, 430, L65

Wang, Y. M. 2000, ApJ, 543, L89

Wang, T. J., Solanki, S. K., Curdt, W., Innes, D. E., & Dammasch, I. E. 2002, ApJ, 574, L101

Williams, D. R., Mathioudakis, M., Gallagher, P. T., Phillips, K. J. H., McAteer, R. T., Keenan, F. P., Rudawy, P., Katsiyannis, A. C. 2002, MNRAS, 336, 747